JOURNAL OF AIRCRAFT
Vol. 32, No. 1, January–February 1995

Flutter Suppression Control Law Design and Testing for the Active Flexible Wing

Vivek Mukhopadhyay*
NASA Langley Research Center, Hampton, Virginia 23681

Design of a control law for simultaneously suppressing the symmetric and antisymmetric flutter modes of a sting-mounted, fixed-in-roll aeroelastic wind-tunnel model is described. The flutter suppression control law was designed using linear quadratic Gaussian theory, and involved control law order reduction, a gain root-locus study, and use of previous experimental results. A 23% increase in the open-loop flutter dynamic pressure was demonstrated during the wind-tunnel test. Rapid roll maneuvers at 11% above the symmetric flutter boundary were also performed when the model was in a free-to-roll configuration.

Nomenclature

A, B = control law state-space matrices
C, D = control law output matrices
E = expectation operator
F, G = plant state-space matrices
G_w = gust input matrix
g = gravitational acceleration constant
H = sensor output matrix
q = dynamic pressure, psf
q_f = flutter dynamic pressure, psf
s = Laplace operator
$\ddot{z}$ = accelerometer output, g
δ = control surface angular position, deg

Subscripts
LEI = wing leading-edge inboard
LEO = wing leading-edge outboard
TEI = wing trailing-edge inboard
TEO = wing trailing-edge outboard
tip = wingtip

I. Introduction

A SUMMARY of the NASA/Rockwell Active Flexible Wing (AFW) program is presented in Refs. 1 and 2. In the AFW design, significant aeroelastic deformation is permitted for weight-saving, while relying on feedback control systems to provide rapid roll performance and to suppress aeroelastic instabilities such as flutter using multiple sensors and control surfaces. This article describes a digital flutter suppression system (FSS) design and testing for the AFW aeroelastic model in the Langley Research Center Transonic Dynamics Tunnel (TDT). Within the operating range of the TDT, the sting-mounted AFW aeroelastic model was predicted to have both symmetric and antisymmetric modes of flutter instabilities, in a fixed-in-roll configuration. When the model was in a free-to-roll configuration, only a symmetric mode of flutter instability was predicted. The active flutter suppression system test goals were to demonstrate 1) simultaneous symmetric and antisymmetric flutter suppression for the fixed-in-roll configuration, and 2) symmetric flutter suppression in the free-to-roll configuration. An additional goal was to test a rolling maneuver load alleviation system along with the FSS, above the open-loop flutter boundary. Since the free-to-roll symmetric flutter and the fixed-in-roll symmetric and antisymmetric flutter modes had very similar characteristics, a single FSS control law was designed and demonstrated for both the flutter test configurations, 1 and 2, as stated above. Initial flutter suppression control laws were designed using linear quadratic Gaussian (LQG) theory and order reduction procedures. A parametric analysis and gain root-locus study were employed in order to compensate for phase lag associated with digital implementation and to accommodate uncertainties in flutter frequencies. The control laws were digitally implemented and tested in TDT. Wind-tunnel test results and comparison with analysis are presented and possible reasons for the differences are discussed.

Presented as Paper 92-2095 at the AIAA Dynamics Specialist Conference, Dallas, TX, April 16–17, 1992; received May 12, 1992; revision received March 7, 1994; accepted for publication March 21, 1994.

*Aeroelastic Analysis and Optimization Branch, Structural Dynamics Division, M/S 246. Associate Fellow AIAA.

II. AFW Equations of Motion

The description of the AFW aeroelastic wind-tunnel model and the wingtip ballast stores, including details of the accelerometer sensor positions and multiple control surface actuation capabilities, are provided in Refs. 1 and 2 (see Fig. 1 in Ref. 1). The accelerometer sensors and the control surface locations on the wing-plan form are shown in Fig. 1. The candidate pair of sensors and control surfaces used for the FSS design are also shown. The development of the aeroelastic equations of motion is described in Ref. 3. The equations for the symmetric and antisymmetric motion were developed separately, using 10 flexible modes for each configuration. The flexible mode shapes and natural frequencies were derived from a finite element modal analysis and were corrected using ground vibration test data. Doublet-lattice solution procedure was used to compute unsteady oscillatory aerodynamic forces acting on each mode. The equations also included corrections for control surface effectiveness based on results from the 1989 wind-tunnel test.[2]

A. State-Space Equations

In order to represent the aeroelastic equations in state-space form, the unsteady aerodynamics rational approximation[3] was used with four aerodynamic lag terms for each of the 10 flexible modes. This resulted in 60th-order linear state-space equations, which were then augmented with third-order transfer functions to represent each control surface actuator dynamics derived from ground test of the unloaded control surfaces. A second-order Dryden gust spectrum transfer function, driven by a white noise process was appended to simulate the

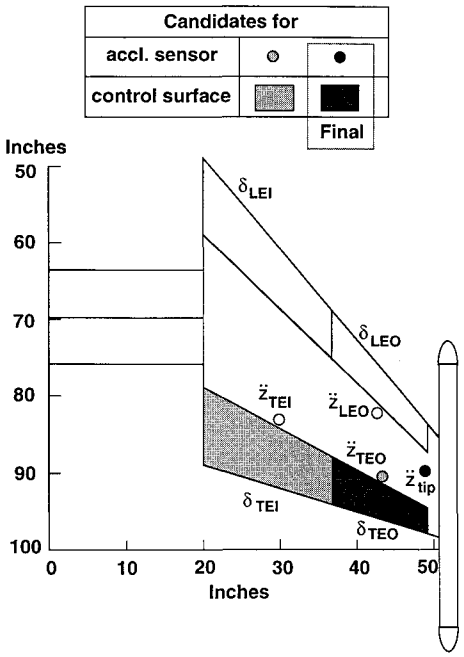

Fig. 1 Accelerometer sensors and control surface locations on AFW wing-plan form.

random vertical gust of the wind tunnel. Thus, complete linear equations of motion of a design plant with two sensors and two actuators at a specified dynamic pressure were expressed by 68th-order state-space equations in the form

$$\frac{dx}{dt} = Fx + Gu + G_w w \tag{1}$$

and

$$y = Hx + v \tag{2}$$

where x is the state vector, u is the control input vector, w is the gust input noise, y is the accelerometer sensor output vector, and v is the measurement noise vector. Equations (1) and (2) were scaled such that the units of the control inputs were in degrees, the units of the sensor outputs were in g (acceleration due to gravity), and the gust input unit was in ft/s.

B. Open-Loop Dynamic Pressure Root-Locus

Using these state-space mathematical models at six dynamic pressures, q = 100, 150, 200, 250, 300, and 350 psf, the flexible-mode root-locus with dynamic pressure were studied. The open-loop, dynamic pressure root-locus of the first four flexible antisymmetric modes in the fixed-in-roll configuration is shown in Fig. 2. This figure indicated that the second and third flexible antisymmetric mode frequencies nearly coalesced to produce the flutter instability in the fixed-in-roll configuration, and the unstable mode was primarily wingtip torsion. The analytical open-loop antisymmetric flutter dynamic pressure was estimated to be 233 psf at 10.9 Hz. The open-loop, dynamic pressure root-locus for the first four flexible symmetric modes are shown in Fig. 3. Here, also the second and third flexible symmetric mode frequencies nearly coalesced to produce another flutter instability, and the unstable mode was again primarily wingtip torsion. The sixth and seventh symmetric flexible mode frequencies also tended to come close (not shown in Fig. 3). At Mach 0.5, the analytical open-loop symmetric flutter dynamic pressure was estimated to be 248 psf at 11.2 Hz. Although the antisymmetric and symmetric flutter modes had very similar characteristics for the fixed-in-roll configuration, the antisymmetric flutter

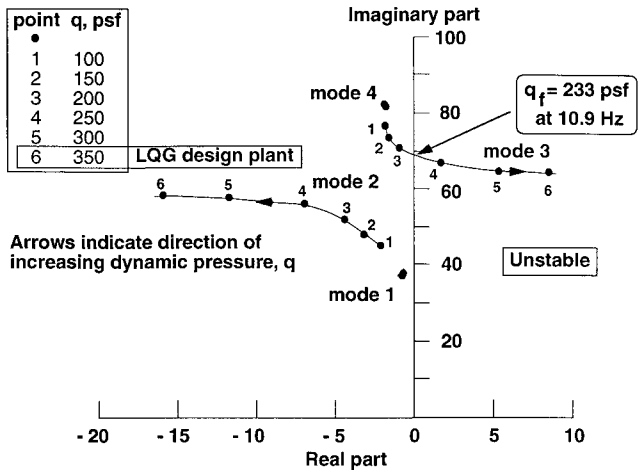

Fig. 2 Open-loop dynamic pressure root-locus for first four antisymmetric modes in fixed-in-roll configuration at Mach 0.5.

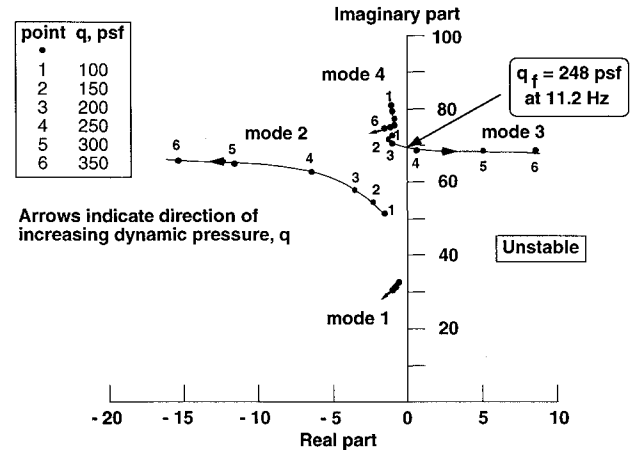

Fig. 3 Open-loop dynamic pressure root-locus for the first four symmetric modes at Mach 0.5.

instability occurred at a lower dynamic pressure and was considered most critical in the control law design process, which is described next. The sixth and seventh mode interaction was compensated for using notch filters.

III. Control Law Design

The design objective of the flutter suppression control laws was to develop low-order robust digital control laws that would simultaneously suppress symmetric and antisymmetric flutter in the fixed-in-roll configuration with allowable control surface activity. The FSS control law design goal was to increase the lowest open-loop flutter dynamic pressure by 30%. Control laws were also required to operate in conjunction with rapid roll maneuver control laws in the free-to-roll configuration. In this configuration the goal was to test a rolling maneuver load alleviation system along with the FSS above the open-loop flutter boundary. The control-surface activity was required to be minimal. The maximum permissible control surface rms deflection and rates were 1.0 deg and 70 deg/s, respectively (at 11.2-Hz flutter frequency). Singular value based multiplicative stability margins corresponding to ±4-dB gain margin and ±30-deg phase margin were required over the entire test dynamic pressure range to account for modeling errors and uncertainties. From the 1989 test[2] the antisymmetric flutter frequency was known to be 1.8 Hz below the analytical value. The control law was also required to be sufficiently robust to compensate for this difference. Sensitivity analysis was also required to assure that likely modeling errors and uncertainties can be accommodated by the flutter suppression control laws.

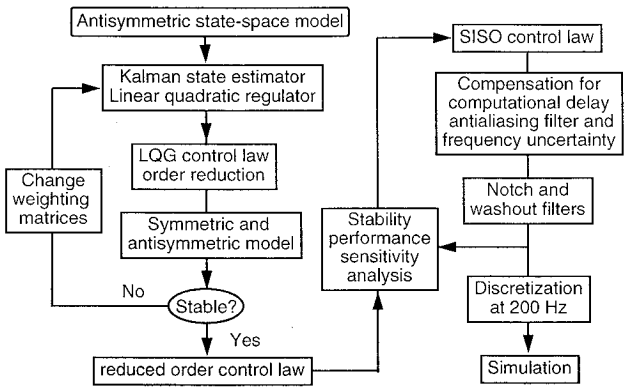

Fig. 4 Control law design procedure block diagram.

The control law design procedure block diagram is shown in Fig. 4. The initial control laws for the antisymmetric flutter suppression were designed using linear quadratic Gaussian theory and subsequent control law order reduction through an iterative procedure. Since the symmetric and antisymmetric flutter modes had very similar characteristics for the fixed-in-roll configuration (see Figs. 2 and 3), a single second-order FSS control law was found to suppress both the flutter modes of the nominal design model. After performance analysis this control law was simplified and improved in order to compensate for the uncertainty in flutter frequencies and phase lags associated with digital implementation. After the addition of a notch filter and a washout filter, the final control law was discretized to operate at 200-Hz sampling rate for digital implementation and simulation. This control law used the $\ddot{z}_{tip}$ pair of accelerometers and the TEO pair of control surfaces on the right and left wings. The details are presented next.

A. Design Plant Model

The full 68th-order antisymmetric state-space equations at q = 350 psf for the fixed-in-roll configuration was used as the design plant model, since from the analysis and the 1989 test, the antisymmetric flutter mode was found to be most critical and was encountered at a lower dynamic pressure, than the symmetric flutter mode. The accelerometer sensors and control surfaces were selected based on the frequency response analysis of the open-loop system. The $\ddot{z}_{TEO}$ and $\ddot{z}_{tip}$ accelerometer responses were predominant at the wingtip torsion frequencies due to the excitation from TEI and TEO control surfaces. In addition, the $\ddot{z}_{tip}$ sensor exhibited relatively low response at frequencies above 25 Hz. Therefore, $\ddot{z}_{TEO}$ and $\ddot{z}_{tip}$ accelerometer sensors and TEI and TEO control surfaces were initially studied as candidates for measurement inputs and control outputs, respectively (see Fig. 1).

B. Full-Order LQG Design

A full-order LQG control law was designed using the design plant model state-space Eqs. (1) and (2). The full-order LQG control law, which is given by Eqs. (3) and (4), minimizes a weighted quadratic cost function defined by $E[\boldsymbol{y}^T Q_1 \boldsymbol{y} + \boldsymbol{u}^T Q_2 \boldsymbol{u}]$, where Q_1 and Q_2 are the plant output and control input weighting matrices[4,5]:

$$\frac{d\boldsymbol{x}_c}{dt} = A_0 \boldsymbol{x}_c + B_0 \boldsymbol{y} \tag{3}$$

$$\boldsymbol{u} = C_0 \boldsymbol{x}_c \tag{4}$$

where

$$A_0 = [F - B_0 H + G C_0]$$

$$B_0 = P H^T R_v^{-1}$$

$$C_0 = Q_2^{-1} G^T S$$

The matrices B_0 and C_0 are the Kalman state estimator gains and the full-state optimal regulator gains, respectively. The matrices P and S are the positive definite solution of the steady-state dual matrix Riccati equations, given by

$$FP + PF^T + G_w R_w G_w^T - P H^T R_v^{-1} H P = 0$$

$$SF + F^T S + H^T Q_1 H - S G Q_2^{-1} G^T S = 0$$

where R_w and R_v denote the intensity matrices of the gust input and measurement Gaussian white noise processes, w and v, respectively. To obtain the LQG control law, full-state optimal regulator gain matrix C_0 was first determined using a unit output weighting matrix $Q_1 = I$, and a control weighting matrix $Q_2 = 0.001I$, where I is a 2 × 2 identity matrix. Then the Kalman state estimator gain matrix B_0 was determined using $R_w = 0$ and $R_v = I$. The final selection of these weighting and noise intensity matrices for the full-order control law, and the subsequent order reduction process were determined after several design iterations, until a stabilizing low-order controller was found for both the nominal antisymmetric and symmetric plant model at 350 psf. The control law order reduction process is described next.

C. Order Reduction

The full 68th-order LQG control law given by Eqs. (3) and (4) was first block-diagonalized, and then reduced to 11th order by residualization of all the damped modes above 19 Hz. Equations (3) and (4) in block-diagonalized form, are shown in Eqs. (5) and (6), where the vector $\boldsymbol{x}_{c1}$ represents the retained states, and the vector $\boldsymbol{x}_{c2}$ represents the remaining states associated with the damped higher frequency dynamics:

$$\frac{d}{dt}\begin{Bmatrix}\boldsymbol{x}_{c1}\\ \boldsymbol{x}_{c2}\end{Bmatrix} = \begin{bmatrix}A_{01} & 0\\ 0 & A_{02}\end{bmatrix}\begin{Bmatrix}\boldsymbol{x}_{c1}\\ \boldsymbol{x}_{c2}\end{Bmatrix} + \begin{bmatrix}B_{01}\\ B_{02}\end{bmatrix}\boldsymbol{y} \tag{5}$$

$$\boldsymbol{u} = [C_{01} \quad C_{02}]\begin{Bmatrix}\boldsymbol{x}_{c1}\\ \boldsymbol{x}_{c2}\end{Bmatrix} \tag{6}$$

In the residualization procedure, only the steady-state part of the stable higher frequency dynamics in Eq. (5) were retained. This was accomplished by setting the state derivative $d\boldsymbol{x}_{c2}/dt$ to 0, and solving for $\boldsymbol{x}_{c2}$, provided the matrix A_{02} is nonsingular.[4] The reduced state-space model of the control law is given by Eqs. (7) and (8):

$$\frac{d\boldsymbol{x}_c}{dt} = A\boldsymbol{x}_c + B\boldsymbol{y} \tag{7}$$

$$\boldsymbol{u} = C\boldsymbol{x}_c + D\boldsymbol{y} \tag{8}$$

where

$$\boldsymbol{x}_c = \boldsymbol{x}_{c1}, \quad B = B_{01}, \quad C = C_{01}, \quad D = -C_{02}A_{02}^{-1}B_{02}$$

This procedure introduced a direct feed through matrix D in Eq. (8). The residualized 11th-order control law was subsequently reduced to a second-order control law by balanced realization and truncation of the balanced system. The balanced realization procedure finds a linear transformation in which the control law states have equal controllability and observability properties.[4] The weakly controllable and observable states are then truncated. Even with the elimination of these states, the resulting set of equations retained the most important input-output characteristics of the original system.

This second-order, two-input, two-output control law, is given by Eqs. (9) and (10):

$$\frac{dx_c}{dt} = \begin{bmatrix} -5.2 & 64.6 \\ -64.6 & -5.2 \end{bmatrix} x_c + \begin{bmatrix} 1.25 & 1.95 \\ -0.45 & -0.73 \end{bmatrix} \begin{Bmatrix} \ddot{z}_{TEO} \\ \ddot{z}_{tip} \end{Bmatrix} \tag{9}$$

$$\begin{Bmatrix} \delta_{TEI} \\ \delta_{TEO} \end{Bmatrix} = \begin{bmatrix} -0.4 & 2.1 \\ 3.6 & -9.4 \end{bmatrix} x_c + \begin{bmatrix} -0.06 & -0.09 \\ 0.13 & 0.21 \end{bmatrix} \begin{Bmatrix} \ddot{z}_{TEO} \\ \ddot{z}_{tip} \end{Bmatrix} \tag{10}$$

The corresponding Bode diagrams of the four components of this 2 × 2 control law are shown in Fig. 5. This figure indicated that the primary stabilizing gain of this control law was from the sensor $\ddot{z}_{tip}$ to the control surface δ_{TEO}, and the maximum gain was 2.5 deg/g (8 dB) at 10.3 Hz (dashed line in Fig. 5 labeled by $\delta_{TEO}/\ddot{z}_{tip}$). Although this control law stabilized the symmetric and antisymmetric plant models at 350 psf, the step responses contained high-frequency components. With the addition of 25-Hz anti-aliasing filters, modeled by the transfer function $157/(s + 157)$ to each accelerometer channel, the high-frequency components of the step responses were eliminated, but a phase lag was introduced (22 deg at 10 Hz). Moreover, with the addition of $T = 0.005$-s computational delay [modeled by the first-order Pade approximation $(2/T - s)/(2/T + s)$], the system was marginally stable due to additional phase lag (18 deg at 10 Hz). It was also found that, when this control law was reduced to a single-input, single-output (SISO) control law by retaining only the control law input $\ddot{z}_{tip}$ and the output δ_{TEO}, it could also stabilize the nominal design plant. Therefore, this simplified SISO control law was studied further in order to compensate for these phase lags associated with digital implementation, and to accommodate possible uncertainty in the actual flutter frequencies, as mentioned earlier.

D. SISO Control Law

This initial simplified SISO control law Bode plot (dashed line in Fig. 5, labeled by $\delta_{TEO}/\ddot{z}_{tip}$), indicates that at the actual antisymmetric flutter frequency 9.1 Hz, the gain was only 1.35 deg/g. Therefore, this initial simplified control law was improved further via gain augmentation. The required gain level to be maintained over a possible flutter frequency range of 8 to 12 Hz was determined using a gain root-locus analysis. The output gain feedback root-locus of the design plant model at 350 psf, with δ_{TEO} as plant input, and $\ddot{z}_{tip}$ as plant output, is shown in Fig. 6. This root-locus indicated that the open-loop unstable pole (mode 3), near 11 Hz, migrated into the stable left half-plane, with a negative feedback gain of 1.3 deg/g from $\ddot{z}_{tip}$ to δ_{TEO}. However, the actuator poles near 50 Hz become unstable at a gain of 0.75 deg/g. Therefore, a gain

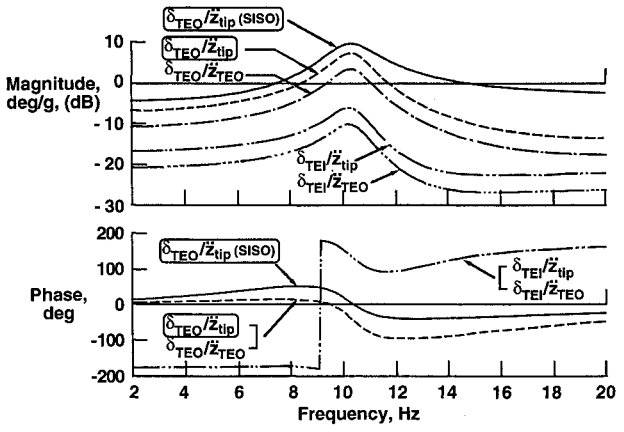

Fig. 5 Bode diagram of reduced second-order control laws.

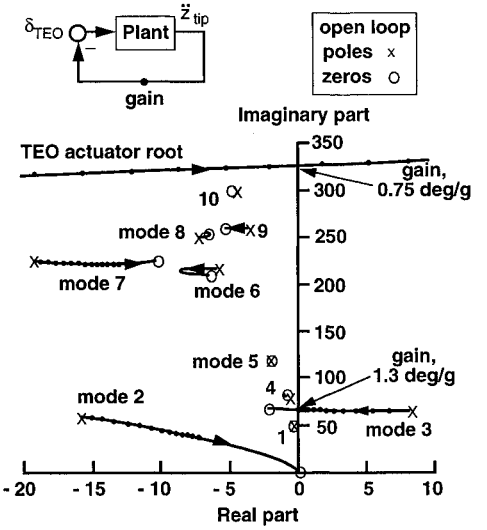

Fig. 6 Gain root-locus plot for negative feedback gain from $\ddot{z}_{tip}$ to δ_{TEO} for antisymmetric fixed-in-roll configuration at 350 psf (× = poles, ○ = zeros, • indicates gain increment by 0.1).

level of at least 1.3 deg/g in the 8–12-Hz frequency range, with subsequent gain attenuation at higher frequencies to well below 0.75 was necessary to stabilize the system, and accommodate the possible difference between the analytical and experimental flutter frequencies. In addition, compensation for the phase lag effects of the anti-aliasing filter and one cycle computational delay was also required as mentioned earlier. The total phase lag introduced by these two effects, was about 40 deg at the frequency 10 Hz.

The gain and phase compensations were achieved by varying the three elements of C and D in the SISO control law, and studying the gain and phase diagrams and the closed loop stability responses. An increase in C_1 and decrease in $|C_2|$ resulted in a desirable phase increase at low frequencies. An increase in D changed the phase (towards zero) at high frequencies, which was also beneficial. These three parameters were varied, until a gain-level near 1.3 deg/g (2.3 dB) was maintained over the frequency range 8–12 Hz, and necessary phase lead over 40 deg was obtained. The high-frequency gain was increased up to only 0.63 deg/g. The real part of the control law complex pole was also moved from -5.2 to -6.0 to achieve a wider gain range. This modified SISO control law is given by Eqs. (11) and (12), assuming negative feedback:

$$\frac{dx_c}{dt} = \begin{bmatrix} -6.0 & 64.6 \\ -64.6 & -6.0 \end{bmatrix} x_c + \begin{bmatrix} 1.95 \\ -0.73 \end{bmatrix} \ddot{z}_{tip} \tag{11}$$

$$\delta_{TEO} = [14.4 \quad -3.1] x_c + 0.63 \ddot{z}_{tip} \tag{12}$$

The corresponding Bode diagram is also shown in Fig. 5 by solid lines, and are labeled $\delta_{TEO}/\ddot{z}_{tip}$ (SISO). The complex poles and zeros of this control law were $-6 \pm j64.6$ and $-30 \pm j56$, respectively. A second-order notch filter, given by the transfer function $(s^2 + 42s + 44100)/(s^2 + 84s + 44100)$ was added to increase the symmetric model gain margin to 6 dB, near 33 Hz at 350 psf. This notch filter attenuated a 33 Hz lightly damped oscillation due to the interaction of the sixth and seventh symmetric flexible modes, as mentioned in Sec. II. A first-order washout filter, given by the transfer function $s/(s + 6)$, was also added to remove any steady-state input bias to the sensor signal.

E. Discretization

The resulting 5th-order SISO control law in Laplace domain was discretized using the Tustin transformation $z = (1 + sT/2)/(1 - sT/2)$, where T is the sampling interval. For the 200-Hz sampling rate used by the digital controller, $T = 0.005$ s.

With the Tustin transformation at this sampling rate, the Bode diagrams in the Laplace domain and the discrete domain were almost identical below 15 Hz. Hence, no frequency warping corrections were applied. For digital implementation[1,2] of this digital control law for suppressing symmetric and antisymmetric flutter simultaneously, the outputs from the left and right wingtip accelerometers were passed through 25-Hz analog anti-aliasing filters, and converted into digital data at a sampling rate of 200 Hz. The digital controller separated the data into symmetric and antisymmetric components, computed the digital control law outputs, and then distributed the processed feedback signals to the right and left TEO actuators. The process involved 0.005-s computational delay.

F. Dynamic-Pressure Root-Locus

The closed-loop dynamic pressure root-locus plots for the first four antisymmetric and symmetric modes are shown in Figs. 7 and 8, respectively. These figures indicate that closed-loop stabilization was achieved by active damping augmentation of mode 3, and closed-loop frequency decoupling due to lowering of mode 2 frequency to about 6.8 Hz, but with reduced damping. Both the symmetric and antisymmetric models were predicted to be stable up to dynamic pressure q = 350 psf, but the damping ratio for the antisymmetric case was only of the order 0.005. The damping ratio was only of the order 0.010 at 250 psf.

G. Sensitivity Studies

The closed-loop system sensitivity was studied by perturbing the second and third modal frequencies in the state-space block-diagonalized plant model by ±10%, and the nominal gains by ±4 dB at q = 250 psf and examining the closed-loop system step responses, for all possible combinations. These studies indicated that the design could accommodate simultaneous gain and frequency changes for all cases except when the second and third mode frequencies were perturbed to approach each other. Sensitivity studies were also done using the state-space model with and without the 25-Hz anti-aliasing filters, with and without one cycle delay, with additional delays, and with ±6 dB gain perturbations at 250 psf. These studies indicated that the symmetric configuration could tolerate one additional delay (or phase lag of 18 deg at 10 Hz) at half the nominal gain, but the antisymmetric configuration would become unstable with an 11-Hz oscillation. The phase and gain margin comparisons with the experimental results, described in the next section, indicated that this particular situation may have been encountered during the experiment. The gain loss was apparent from the Bode diagrams derived from the wind-tunnel test results.

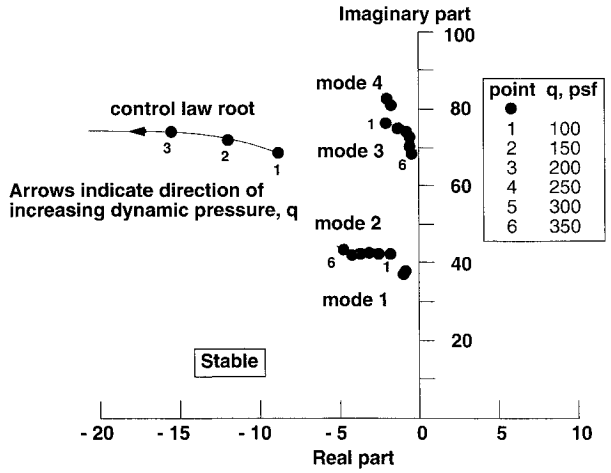

Fig. 7 Closed-loop dynamic pressure root-locus for first four antisymmetric modes in fixed-in-roll configuration at Mach 0.5.

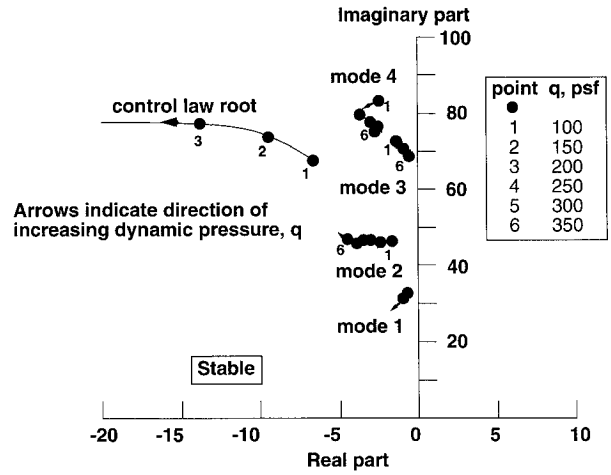

Fig. 8 Closed-loop dynamic pressure root-locus for the first four symmetric modes at Mach 0.5.

IV. Summary of Test Results

A. Open-Loop Flutter

Based on examination of the peak-hold data obtained during the wind-tunnel test with the tip ballast store coupled, the open-loop (OL) flutter dynamic pressures were as follows: The fixed-in-roll OL antisymmetric flutter was at a dynamic pressure of 219 psf, at a frequency of 9.1 Hz. The free-to-roll OL symmetric flutter was at a dynamic pressure of 235 psf, at a frequency of 9.6 Hz. These experimental antisymmetric and symmetric OL flutter dynamic pressures were, respectively, 14 and 13 psf below the predicted values, and the flutter frequencies were, respectively, 1.8 and 1.6 Hz below the predicted values. The differences between analytical and experimental values were possibly due to approximations involved in modeling the unsteady aerodynamic forces and flexible structural mode shapes.

B. Open-Loop Frequency Responses

Figures 9 and 10 show the OL frequency responses of $\ddot{z}_{tip}$ due to δ_{TEO} from analysis and experiment at 250 psf, for the antisymmetric mode (fixed-in-roll) and symmetric mode case, respectively. Since at this dynamic pressure the OL plant was unstable, the frequency responses were computed from closed-loop (CL) experimental data, using the controller performance evaluation (CPE) procedure.[6,7] Figure 9 indicates that for the antisymmetric mode in the critical frequency band from 7 to 12 Hz, the experimental response magnitudes were significantly lower, ranging from 10 to 25 dB. Above 12 Hz, the magnitudes were lower by 6–8 dB, and the phase angles lagged by 10–20 deg. The gain and phase diagrams appeared to be shifted towards lower frequency by 1.8 Hz. Figure 10 indicates that for the symmetric mode in the critical frequency

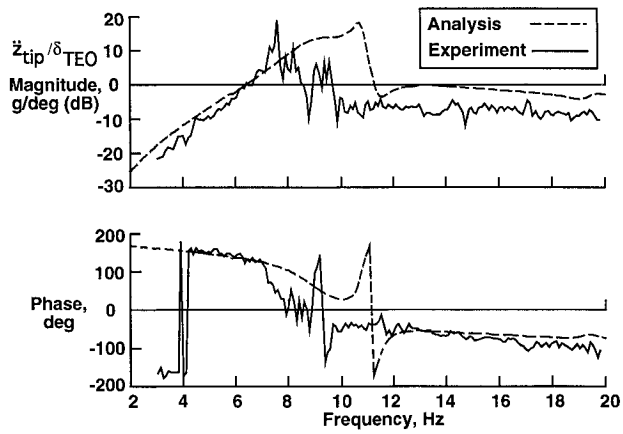

Fig. 9 Comparison of $\ddot{z}_{tip}/\delta_{TEO}$ Bode diagram at 250 psf, antisymmetric fixed-in-roll configuration.

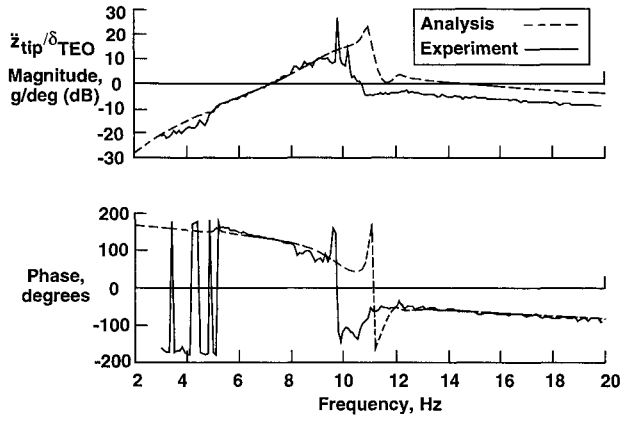

Fig. 10 Comparison of $\ddot{z}_{tip}/\delta_{TEO}$ Bode diagrams at 250 psf, symmetric configuration.

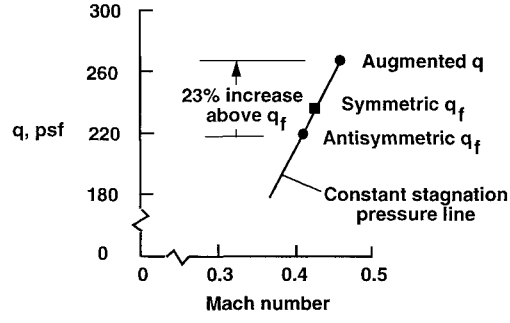

Fig. 11 Summary of results for fixed-in-roll FSS wind-tunnel test.

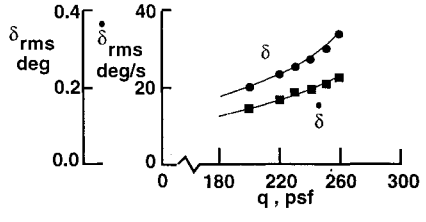

Fig. 12 Maximum TEO control surface deflection and rate demands during simultaneous symmetric and antisymmetric flutter suppression.

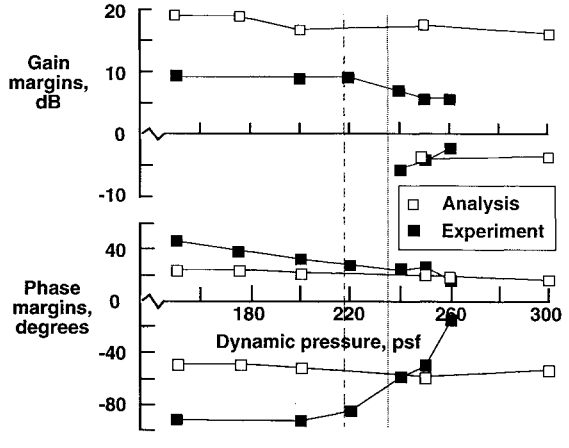

Fig. 13 Gain and phase margin comparison (antisymmetric, fixed-in-roll).

band from 8 to 12 Hz, the experimental response magnitudes were significantly lower, ranging from 6 to 25 dB. Above 12 Hz, the magnitudes were lower by about 6 dB, whereas the phase angles were nearly equal. The gain and phase diagrams appeared to be shifted towards lower frequency by 1.6 Hz. Note, that in each phase diagram, the 180-deg crossing occurs near the respective OL flutter frequencies, and the difference between their predicted and experimental values is quite ap-

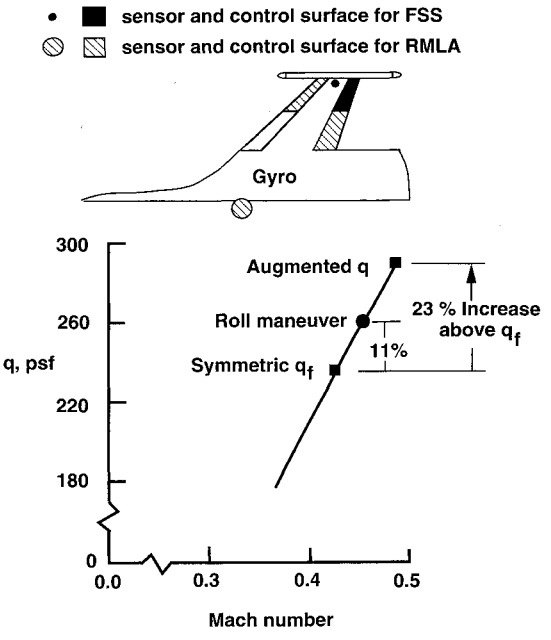

Fig. 14 Summary of results for free-to-roll RMLA/FSS wind-tunnel test.

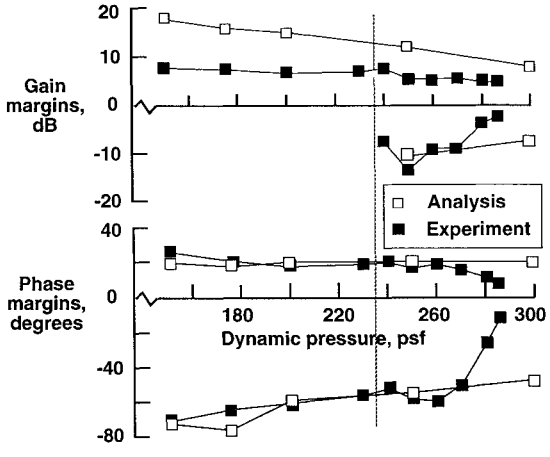

Fig. 15 Gain and phase margin comparison (symmetric).

parent. The differences between analytical and experimental frequency responses of $\ddot{z}_{tip}$ due to δ_{TEO} was primarily due to approximate modeling of the unsteady aerodynamic forces with attached potential flow assumption.

C. Closed-Loop Tests

The active flutter suppression test results are summarized in Figs. 11–15. Figure 11 shows the wind-tunnel test dynamic pressures vs the freestream Mach number, in the fixed-in-roll configuration when both the antisymmetric and symmetric flutter modes were being suppressed simultaneously. With both the symmetric and antisymmetric FSS control laws operating, the CL system was stable only up to $q = 270$ psf, at Mach 0.46. This augmented q represents a 23% increase over the OL antisymmetric flutter q_f.

The rms deflection and deflection rate of the right and left side TEO control surface were computed from the data sampled at 200 Hz at each fixed-in-roll FSS test condition. If the value of the right and left differed, the maximum is plotted in Fig. 12. The maximum rms deflection and rates were less than 0.4 deg and 25 deg/s, respectively. These maximum rms deflection and rate demands of the actuators were well below the maximum allowable values of 1 deg and 75 deg/s as stated earlier in this article.

The experimental Nyquist-diagrams were plotted for the antisymmetric fixed-in-roll configuration using the CPE tech-

nique.[7] The gain- and phase-margins were estimated from these Nyquist plots, and compared with the corresponding analytical quantities in Fig. 13. The vertical dashed line at 219 psf denotes the antisymmetric flutter boundary crossing. Beyond the symmetric flutter boundary at 235 psf denoted by vertical dotted line, where both the flutter modes were being suppressed, the negative phase margin deteriorated rapidly. The negative gain and phase margins at the high frequency end (above 12 Hz) were primarily responsible for preserving the system stability. The rapid loss of negative stability margin at higher dynamic pressures was probably due to response lag of the loaded actuators and reduced control surface effectiveness to generate nose-down torsion moment. The rapid loss of gain margin was apparent from the experimental Bode magnitude diagram in the 8–12-Hz frequency range as shown in Fig. 9.

Figure 14 shows the wind-tunnel test dynamic pressures vs the freestream Mach number, during the wind-tunnel test, in the free-to-roll configuration. With the symmetric FSS control law operating, the CL system was stable up to $q = 290$ psf, at Mach 0.48. This augmented q represents a 23% increase over the OL symmetric flutter q_f as shown in Fig. 14. This FSS control law also suppressed the flutter when a rolling maneuver load alleviation (RMLA) system[8] was tested with rapid roll maneuvers at $q = 260$ psf, 11% above the OL symmetric flutter boundary. This RMLA control law used LEO and TEI control surfaces, and so the interaction with the FSS control law was minimal.

The experimental Nyquist-diagram-based gain- and phase-margins were also estimated for the symmetric free-to-roll configuration using the CPE technique.[7] These estimates were compared with the corresponding analytical quantities in Fig. 15. The vertical dashed line at 235 psf denotes the symmetric flutter boundary crossing. The analytical and experimental gain margins were above ± 6 dB up to 270 psf, beyond which experimental values deteriorated rapidly. The analytical positive phase margins (at or below 7 Hz) were about 20 deg, but the negative phase margins (at or above 12 Hz) were well above 45 deg. The analytical phase margins were close to experimental results up to about 270 psf, beyond which experimental values deteriorated rapidly. Again, the negative gain and phase margins at the high-frequency end (above 12 Hz) were primarily responsible for preserving the system stability. The rapid loss of gain margin was apparent from the experimental Bode magnitude diagram in the 8–12-Hz frequency range as shown in Fig. 10.

V. Conclusions

A flutter suppression control law for the active flexible wing model was designed using TEO actuators and wingtip accelerometer sensors. The basic stabilization mechanism of the feedback control law could be interpreted as small acceleration gain feedback below the flutter frequency that reduced the bending mode frequency, and a suitable gain feedback with appropriate phase lag above the flutter frequency that provided torsion mode damping, depending on the ability of the control surface to generate lift and a nose-down torsion moment, respectively. The control law was digitally implemented and tested in a wind tunnel. Simultaneous suppression of symmetric and antisymmetric flutter modes in close proximity was demonstrated to 23% above the open-loop antisymmetric flutter boundary when the model was in a fixed-in-roll configuration. Symmetric flutter suppression system operating simultaneously with a rolling maneuver load alleviation system was tested to 23% above the open-loop symmetric flutter boundary, when the model was in a free-to-roll configuration. With this combined system, rapid roll maneuvers were also performed at 11% above the symmetric flutter boundary. The performance of the control law was less than predicted, possibly due to the following reasons. The modeling of the unsteady aerodynamic forces due to control surface deflection assuming attached potential flow was inadequate. Rapid loss of negative stability margin occurred at higher dynamic pressures, due to response lag of the loaded actuators and reduced control surface effectiveness to generate nose-down torsion moment. In addition, in the fixed-in-roll configuration, the control surfaces were stabilizing the combined effect of symmetric and antisymmetric flutter instabilities, while in the analysis and design these two instabilities were treated as mechanically, structurally, and aerodynamically uncoupled.

References

[1]Perry, B., III, Cole, S. R., and Miller, G. D., "Summary of the Active Flexible Wing Program," Vol. 32, No. 1, 1995, pp. 10–15.

[2]Perry, B., III, Mukhopadhyay, V., Hoadley, S. T., Cole, S. R., Buttrill, C. S., and Houck, J. A., "Digital Implementation, Simulation and Testing of Flutter-Suppression Systems for the Active Flexible Wing Wind-Tunnel Model," AIAA Paper 90-1074, April 1990.

[3]Buttrill, C. S., Bacon, B. J., Heeg, J., and Houck, J. A., "Simulation and Model Reduction for the AFW Program," AIAA Paper 92-2081, April 1992.

[4]Maciejowski, J. M., *Multivariable Feedback Design*, Addison-Wesley, England, UK, 1989.

[5]Bryson, A. E., Jr., and Ho, Y. C., *Applied Optimal Control*, Hemisphere, Washington, DC, 1975.

[6]Pototzky, A. S., Wieseman, C. D., Hoadley, S. T., and Mukhopadhyay, V., "Development and Testing of Methodology for Evaluating the Performance of Multi-Input/Multi-Output Digital Control Systems," AIAA Paper 90-3501, Aug. 1990.

[7]Pototzky, A. S., Wieseman, C. D., Hoadley, S. T., and Mukhopadhyay, V., "On-Line Performance Evaluation of Multiloop Digital Control Systems," *Journal of Guidance, Control, and Dynamics*, Vol. 15, No. 4, 1992, pp. 878–884.

[8]Woods-Vedeler, J. A., and Pototzky, A. S., "Rolling Maneuver Load Alleviation Using Active Controls," AIAA Paper 92-2099, April 1992.